Available online at www.sciencedirect.com
SCIENCE @ DIRECT®

ELSEVIER

Journal of Nuclear Materials 347 (2005) 192–206

journal of nuclear materials

www.elsevier.com/locate/jnucmat

Thermomechanical effects in a laser IFE first wall

James P. Blanchard [*], Carl J. Martin [1]

University of Wisconsin – Madison, Engineering Physics Department, 1500 Engineering Drive,
Madison, WI 53706-1609, United States

Abstract

Laser fusion chamber walls will experience large, pulsed heat loads at frequencies of several hertz. The heating, consisting of X-rays, neutrons, and ions, occurs over a few microseconds and is deposited volumetrically over the first few microns of the wall. For a reasonable chamber radius, the heating will be such that the surface temperature is a significant fraction of the melt temperature of the wall, and significant plasticity can be expected in ductile wall materials. This paper presents results for the transient temperatures and stresses in a tungsten-coated steel first wall for a laser fusion device. Failure analyses are carried out using both fatigue and fracture mechanics methodologies. The simulations predict that surface cracks are expected in the tungsten, but the cracks will arrest before reaching the substrate if the crack spacing is sufficiently small. In addition, the thermal and stress fields are compared for a laser fusion device with several simulation experiments. It is shown that the simulations can reproduce the peak surface temperatures, but the corresponding spatial distributions of the stress and temperature will be shallower than the reactor case.

1. Introduction

The chamber walls in inertial fusion energy (IFE) devices will experience a harsh set of thermal loads resulting from deposition of energy from target implosions. Hence, the chamber design must account for these effects to ensure adequate wall life. Early wall design efforts will require detailed thermomechanical analyses including all thermal loads, nonlinear material effects, and, in some cases, phase changes due to melting or vaporization.

The analyses presented in this paper have been carried out as part of the high average power laser (HAPL) [1] program. HAPL has focused on solid chamber walls, with the primary candidate being a tungsten-coated steel wall. Hence, the conclusions are specific to this design approach. The heat loads in the HAPL design are delivered to the wall in the form of X-rays, neutrons, and ions, and the majority of their energy is deposited in the first few microns of the wall. In some cases a gas (xenon) is placed in the chamber to absorb some of this heat which is radiated to the wall at a later time, thus effectively spreading the heat load over a longer time and reducing the peak wall temperatures. In all cases, the resulting thermal stresses are expected to be well above the yield stress of the tungsten

---

[*] Corresponding author. Tel.: +1 608 263 0391.
E-mail addresses: blanchard@engr.wisc.edu (J.P. Blanchard), cjmartin@engr.wisc.edu (C.J. Martin).

[1] Tel.: +1 608 265 3957.

0022-3115/$ - see front matter © 2005 Elsevier B.V. All rights reserved.
doi:10.1016/j.jnucmat.2005.08.007

coating, and thus the mechanical design will require consideration of fatigue and fracture to ensure that the steel wall is protected for a lifetime sufficient to provide an economical design for a commercial power plant.

This paper presents an overview of the heat loads expected in a HAPL chamber and a series of thermal and structural analyses for a variety of target yields and chamber sizes. All analyses incorporate temperature-dependent properties and nonlinear material effects (primarily plasticity). Fracture models are also used to assess the likelihood of cracks in the tungsten growing until they reach the steel potentially leading to fracture in the steel or delamination of the tungsten coating.

2. Heat loads and properties

From a thermomechanical perspective, the thermal loads on an IFE chamber wall can be viewed as resulting from X-rays, ions, and neutrons. In laser IFE, the energy carried by each of these is typically on the order of 1%, 29%, and 70%, respectively, though these energy splits will vary somewhat depending on the target design and yield. The X-rays typically arrive to the wall first and deposit their energy within a few nanoseconds. The neutrons arrive after 100–200 ns and are deposited over less than 20 ns. Since the neutrons have fairly long mean free paths, only a small fraction of their energy will be captured in the first wall. The ions arrive last, with deposition beginning after about 200 ns and continuing over a time span of ≈3 μs. Again, these numbers will vary with chamber size and target characteristics.

A significant design parameter is gas in the chamber. One can protect the chamber wall by filling the chamber with gas (xenon, for instance) at tens of mTorr pressure (or greater). This gas will stop some of the ions and X-rays before they reach the wall reducing the peak temperature of the first wall surface. The heat absorbed by the gas will then be re-radiated to the wall over a longer time period (typically hundreds of microseconds), effectively spreading the heat deposition over a longer time period and reducing the peak heat flux and wall surface temperature. As an example, 10 mTorr xenon gas in a 6.5 m radius laser IFE chamber will typically stop about 20% of the ion energy and about 9% of the X-ray energy before it reaches the wall.

The X-ray energies are as high as 100 keV, with the bulk falling below 10 keV. Hence deposition of the X-ray energy largely occurs within the first micron of the surface. The ions created by the target burn have energies as high as 10 MeV, with the bulk falling below a few MeV. Their energy is typically deposited over a few microns. The so-called debris ions, initially present in the target and accelerated by the burn, have energies as high as 20 MeV, with the bulk falling below 200 keV. Their energy is deposited over about 1 μm.

Table 1
Characteristics of energy deposited in chamber wall as a result of a single laser target implosion

Type	Fraction of yield	Max energy (keV)	Arrival time (ns)	Pulse width (ns)
X-rays	0.01	100	0	1
Neutrons	0.70		160	20
Burn ions	0.12	25000	200	800
Debris ions	0.17	15000	1000	2750

These data are summarized in Table 1. As will be shown later, there is a local peak in the chamber wall temperature as a result of the X-ray fluence, but the global peak temperature occurs near the end of the ion arrival period.

3. Analytical models

The thermal and stress fields encountered in an IFE chamber will be exceedingly complex. The thermal fields result from volumetric heating rates with complex temporal and spatial variation resulting from the energy spectra of the ions born in the target. The thermal fields are further complicated by the temperature-dependent thermal properties. In cases where melting or vaporization occurs, the situation is even more difficult. Similarly, the stress fields are complex as a result of significant nonlinearity in the material properties resulting from plastic deformation and temperature-dependent properties. However, analytical models of simplified systems can still be quite valuable for initial scoping studies and for testing numerical models ultimately used for design. In this section we present analytical models for several cases relevant to IFE chambers, beginning with a simple base line, 1D stress model, followed by refinements necessary for modeling certain situations.

The base case considers a solid restrained from deformation in two dimensions and without constraint in the third dimension. The lack of constraint in the third dimension is a result of the free surface. The full constraint in the other dimensions assumes that the thermal field is shallow relative to the depth of the structure, so that cold material below the surface restrains motion of the heated material in that shallow layer. A previous paper [2] provides the temperature (T) and stresses (σ) under these assumptions:

$$T = \frac{-2q}{k}\sqrt{\frac{\kappa t}{\pi}},$$
$$\sigma_{yy} = \sigma_{zz} = \frac{-2qE\alpha}{(1-\nu)k}\sqrt{\frac{\kappa t}{\pi}}, \tag{1}$$
$$\sigma_{xx} = 0,$$

where q is the surface heat flux, k is the thermal conductivity, κ is the thermal diffusivity, E is the elastic modulus, ν is Poisson's ratio, and α is the thermal expansion coefficient. The stresses are all normal stresses and the 'x' direction is normal to the surface and the 'y' and 'z' directions are parallel to the surface. This result provides a baseline estimation of the surface stresses induced by rapid surface heating. It assumes isotropic material properties, spatial uniformity of the applied heat, no volumetric heating below the surface, and ignores both elastic and thermal waves. It also ignores plastic deformation. Since many of the HAPL cases feature prominent plasticity, this model is only useful for predicting the onset of plastic deformation, but not for predicting the stress.

Since many scientists are accustomed to referring to the fluence deposited in a single pulse, we can replace the heat flux and time with fluence, according to $F = qt$. In this case, the stresses are given by

$$\sigma_{yy} = \sigma_{zz} = \frac{-2FE\alpha}{(1-\nu)k}\sqrt{\frac{\kappa}{\pi t}},$$
$$\sigma_{xx} = 0. \tag{2}$$

Most surface heating actually deposits heat volumetrically within a thin layer near the surface. A typical model for volumetric heating resulting from energy impinging on a surface is

$$Q''' = A\mathrm{e}^{-\gamma x}, \tag{3}$$

where Q''' is the volumetric heating, A is a constant, γ is the attenuation coefficient, and x is the distance from the surface. To provide the same total heat input as a true surface heating flux q, we must enforce $A = q\gamma$ or $A = Ft\gamma$. The surface temperature resulting from volumetric heating of this type is [2]

$$T_{\text{surface}} = \frac{2F}{k}\sqrt{\frac{\kappa}{\pi t}}\left[1 - \frac{\sqrt{\pi}}{2\zeta}\{1 - \mathrm{e}^{\zeta^2}\mathrm{erfc}(\zeta)\}\right], \tag{4}$$

where $\zeta = \gamma\sqrt{\kappa t}$, representing the ratio of the diffusion length in time t to the characteristic deposition length, and $\eta = x\gamma$. The stresses provided in Eq. (1) can be corrected by the factor in square brackets in Eq. (4), giving

$$\sigma_{yy} = \sigma_{zz} = \frac{-2FE\alpha}{(1-\nu)k}\sqrt{\frac{\kappa}{\pi t}}\,[1 - \mathrm{e}^{\zeta^2}\mathrm{erfc}(\zeta)],$$
$$\sigma_{xx} = 0. \tag{5}$$

In some cases, the energy deposition is fairly uniform over some fixed depth L. In this case, the surface temperature is given by [3]

$$T_{\mathrm{s}} = \frac{F}{\rho c_{\mathrm{p}} L}\left\{1 - 4i^2\mathrm{erfc}\left(\frac{L}{2\sqrt{\kappa t}}\right)\right\},$$
$$i^2\mathrm{erfc}(z) = \frac{1}{4}\mathrm{erfc}(z) - \frac{z}{2\pi}\exp(-z^2) + \frac{z^2}{2}\mathrm{erfc}(z), \tag{6}$$

where ρ is the density and c_p is the heat capacity. And the corresponding stresses are given by

$$\sigma_{yy} = \sigma_{zz} = \frac{-FE\alpha}{\rho c_{\mathrm{p}} L(1-\nu)}\left\{1 - 4i^2\mathrm{erfc}\left(\frac{l}{2\sqrt{\kappa t}}\right)\right\}, \tag{7}$$
$$\sigma_{xx} = 0.$$

We can use the above formulas to estimate the stresses and temperatures expected in a tungsten-coated chamber wall as a result of the thermal loading from a laser IFE target. The results are presented in Table 2. The properties used in this analysis are given in Appendix A. The maximum temperatures resulting from the X-ray and burn ion depositions are calculated assuming an initial temperature of 400 °C. The maximum temperature due to the debris ions is calculated assuming that the initial temperature is the maximum temperature due to the burn ions, since one is assumed to start as the other is completed. The results in this table indicate that the combined heating from the burn and debris ions will give higher temperatures than the X-ray heating.

Table 2
Estimated wall temperatures resulting from a 150 MJ target implosion in a 7 m radius chamber with no gas in the chamber

Type of deposition	X-rays (exponential)	Burn ions (uniform)	Debris ions (uniform)
Characteristic deposition length (μm)	2	10	1
Deposition time (ns)	1	800	2700
Fluence (J/cm^2)	0.32	2.9	4.0
Maximum temperature (°C)	860	1300	2700

It should be noted that the analytical formulas for stresses are not employed here, because those formulas cannot account for plastic deformation, which is prominent in this analysis.

4. Finite element models

In addition to the closed-form thermal and stress analyses described previously, finite element (FE) thermostructural models were developed. The finite element models were better able to simulate the transient first wall response by incorporating more accurate representations of the loads, boundary conditions, and nonlinear material behaviors. A schematic of the first wall design is illustrated in Fig. 1. All modeling was done in the commercial finite element code ANSYS, and the models discussed in this section used axisymmetric two-dimensional elements with temperature-dependent material properties and elastic–plastic material models. Both the thermal and structural models assume, through appropriate boundary conditions, laterally uniform heating. Stresses and strains calculated with these models were solely the product of thermal loads; i.e. no external mechanical or pressure loads were applied. Very thin elements were used near the surface, in order to accurately resolve the sharp temperature gradients encountered during the pulse. The element thickness increased with distance from the surface in order to reduce the total element count. The minimum element thickness in the results presented in this paper was 40 nm.

For the thermal model, the heat deposited from the X-rays, ions, and neutrons were modeled discretely. The volumetric heat loading and arrival times were dependent on chamber radius, and typical values are shown in Table 1. The heat from each component was applied to the chamber surface over a characteristic depth. The energy was deposited uniformly in the tungsten over a depth of 2 μm from the X-rays, a depth of 10 μm from the burn ions, and a depth of 1 μm from the debris ions. The neutron energy was distributed over the entire volume of tungsten and steel. The total time of the heat pulse was around 3 μs and repeated every 0.2 s. Because this heating was intense and highly localized near the surface of the tungsten, an extremely refined mesh was required near the tungsten surface to accurately predict the thermal gradients in this region. Chamber cooling is simulated using convection on the outside of the steel wall. A convection coefficient of 10^4 W/m^2 °C and fluid temperature of 400 °C were assumed, and 400 °C was used as the initial condition for the thermal analyses. Because the model assumes laterally uniform heating, the sidewall is adiabatic. There is also no heat loss from the tungsten free surface as the entire chamber interior is assumed to be isothermal, and hence no radiation would occur. The temperature-dependent thermal material properties used are listed in Appendix A.

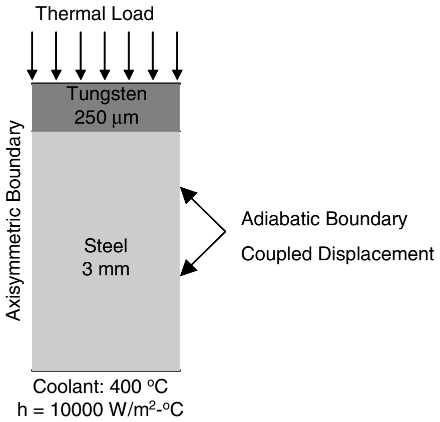

Fig. 1. Wall design and FEA boundary conditions.

The loads input to the transient structural FE model were the temperatures calculated by the thermal model at the various time steps. The side boundary was modeled as a boundary free to expand but not bend. This was simulated by coupling the nodal displacements on the radial edge in the radial direction. Because the yield stress was greatly exceeded in the tungsten, a nonlinear structural analysis was required. The material properties were temperature-dependent, and due to the limited stress–strain data available for tungsten at high temperatures, a simple bilinear material model was used for plasticity. More details of the structural material data used may be found in Appendix A. The yielding of the tungsten surface necessitated that the nonlinear structural analysis proceed stepwise through the transient temperature profile. Due to the short time frames of the thermal loading, creep deformations were not considered.

5. Thermostructural response

Finite element analyses were completed for a variety of chamber radii and armor thicknesses. The first results presented here used a 150 MJ target yield, 7.0 m chamber radius, 250 μm armor thickness, and 3 mm substrate thickness. This armor thickness (250 μm) was chosen to ensure acceptable temperatures and stresses in the steel. First, the complete thermostructural response of the wall at this base line condition will be presented followed by a summary of results at other chamber and wall design points.

The FE simulation of the 150 MJ target implosion in the 7.0 m radius chamber predicted a maximum temperature in the tungsten of 2554 °C as illustrated in Fig. 2. From this figure, it can be seen that the heating was quite localized near the surface. The maximum temperature was 1393 °C at a depth of 10 μm and fell to 849 °C at a depth of 25 μm. The temperature rise at the tungsten steel interface is barely perceptible in the 50 μs time frame of the plot. The armor response to repeated implosions at a 5 Hz repetition rate is illustrated in Fig. 3. The high temperature transients represent only a small fraction of the cycle, and the net temperature increase with each implosion is relatively small.

The high surface temperatures immediately following each implosion produced large thermal stresses that exceeded the yield point of the tungsten. These stresses are parallel to the surface and are the same in all directions. There is no stress perpendicular to the surface. Hence, the stress state can be characterized with a single stress. The parallel and perpendicular plastic strains are of opposite sign and must sum to zero (to conserve volume), so again they can be characterized with a single strain. The results in this paper will present the strains parallel to the surface. The time dependent stresses and plastic strains in the armor are illustrated in Figs. 4 and 5. It appears in this figure that the initial stresses are non-zero, but this is due to the X-ray burst which occurs in the first few nanoseconds. This produces a large compressive stress, accompanied by yielding, which then leads to tensile residual stresses as the surface cools. The temperature rise due to the ion deposition then produces a second compressive stress and additional plastic deformation, followed again by tensile stresses upon cooling. This cycle

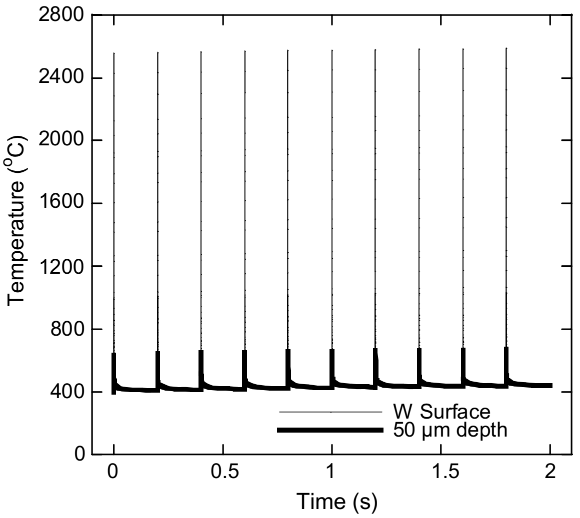

Fig. 3. Transient temperature response in the tungsten armor to ten 150 MJ target implosions in a 7.0 m radius chamber.

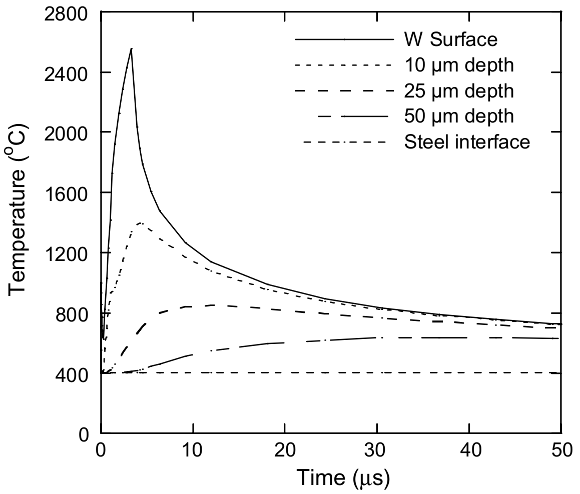

Fig. 2. Transient temperature response of the tungsten armor to the 150 MJ target implosion in a 7.0 m radius chamber.

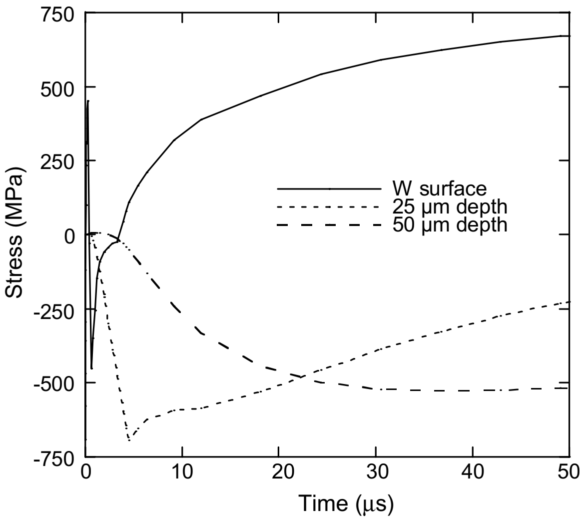

Fig. 4. Transient thermal stress response near the surface of tungsten armor after 150 MJ target implosion.

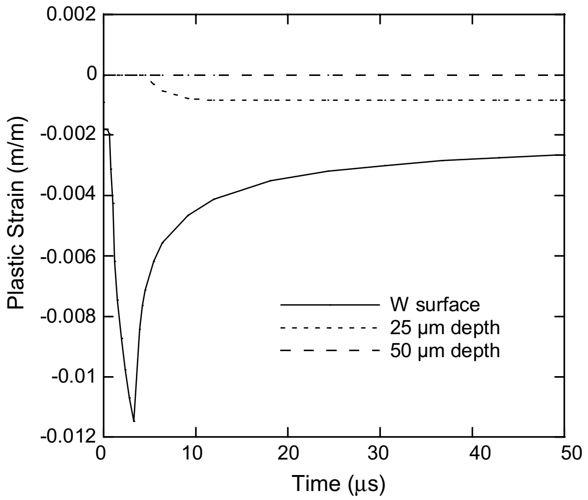

Fig. 5. Transient plastic strain near the surface of tungsten armor after 150 MJ target implosion.

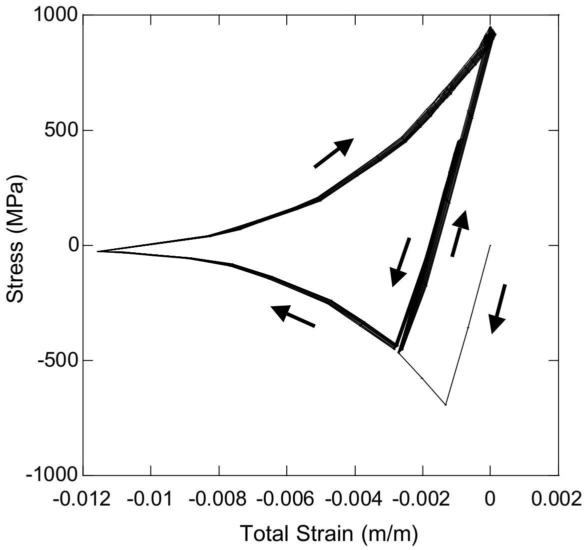

Fig. 6. Cyclic stress–strain response at the surface of tungsten armor for 10 target implosion cycles.

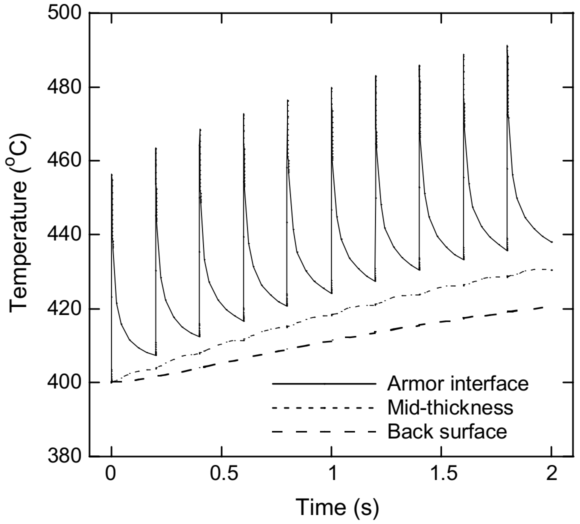

Fig. 7. Transient temperature response of the steel wall to ten 150 MJ target implosions in a 7.0 m radius chamber.

was essentially repeated with each implosion as illustrated in the cyclic stress–strain curve of Fig. 6, which plots the parallel stress versus the parallel strain at the tungsten surface. The material model used here was isotropic hardening, though kinematic hardening was was also tested with little change in the results. In Fig. 6, the stress–strain curves for each of the 10 cycles simulated essentially fall on top of each other, with the slight shift to the left attributable to the gradual heating of the system. The maximum plastic strain at the surface of −0.0115 m/m was reduced to −0.0025 m/m after cool down. At a depth of 25 µm into the armor, the compressive stresses developed at a much slower rate as it took time for the heat to diffuse into the material. A small amount of compressive yielding occurred after the first implosion and remained constant throughout subsequent cycles. Because of the temperature dependence of yield stress, there were variations in the stress level where plastic deformation was initiated during the cycle. At a depth of 50 µm into the armor, no plastic deformation was observed, and the stresses were mainly compressive due to the thermal expansion.

The temperatures in the steel were much lower than those near the surface of the armor. Transient temperatures at the armor interface, the mid-thickness, and back surface of the steel over ten target implosions are illustrated in Fig. 7. At the tungsten/steel interface, temperature spikes of over 55 °C were visible while the back surface temperature increased by 20 °C at a near constant rate over the ten cycles. Only slight temperature oscillations were observed at the mid-thickness of the wall. The rate of the temperature rise from cycle to cycle will be dependent on the heat extraction rate of the wall cooling system, but this will not affect the through the thickness wall thermal gradients which are functions of the heat flux, wall thickness, and thermal conductivity. In this case which used a convection coefficient of 10000 W/m^2 °C, the back surface temperature increased by 38.3 °C after 50 cycles and was reaching a plateau. The peak steel temperature reached 520 °C.

The thermal stresses in the steel were primarily the result of the thermal gradients through the wall thickness. The high temperatures and stresses in the armor had little effect on the steel wall. Stresses at the armor interface, mid surface, and back surface of the steel are plotted as a function of time in Fig. 8. These stresses are well below the yield stress of the steel, which is 850 MPa at 500 C. The highest stresses occurred at the interface with the tungsten where the steel temperatures were highest. The stress here was compressive and closely followed the temperature history. Over the 10 cycles, the maximum stress increased from −175 MPa to −200 MPa as the thermal gradient across the wall increased. The through-thickness stress distribution after 50 target implosions is illustrated in Fig. 9. These stresses, computed at the time of the maximum thermal gradient through the wall, show a large stress gradient in the 0.2 mm of material adjacent to the armor due to the transient heating. The maximum tensile and compressive stress levels after the 50th implosion increased 15 MPa over those after the 10th implosion due to the gradual heating. By the 50th cycle, the temperature had nearly leveled-off, and no further significant stress increase would be expected. The magnitude of the compressive stress at the armor interface was over four times higher than the maximum tensile stress in the steel, and the steel at the interface remained in compression throughout the entire cycle. These stress levels are well within the allowable stresses as defined by the ASME Boiler and Pressure Vessel Code.

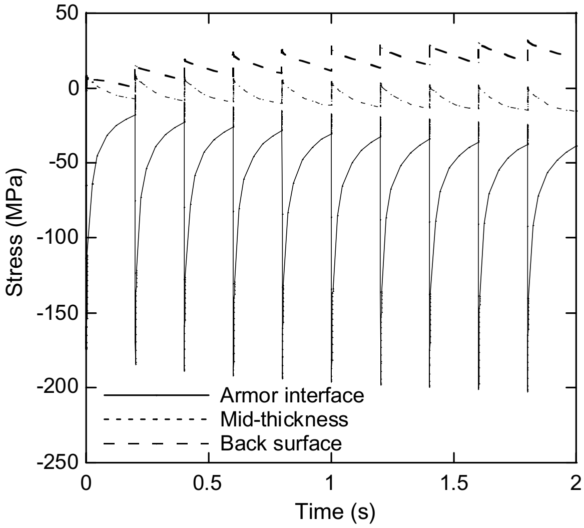

Fig. 8. Transient thermal stresses in the steel wall resulting from ten 150 MJ target implosions.

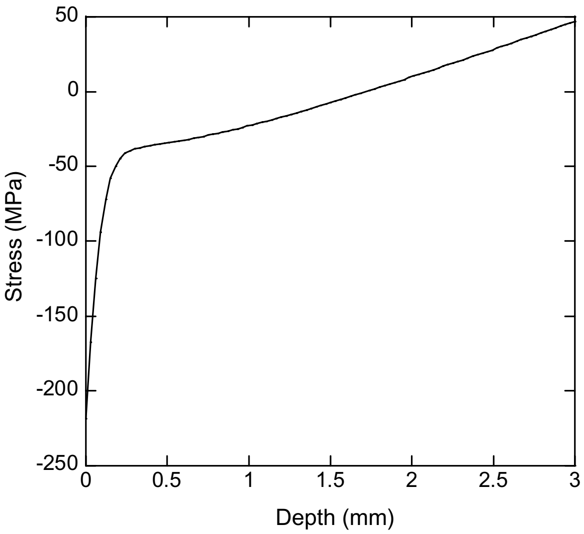

Fig. 9. Thermal stresses distribution through the steel wall thickness after 50 target implosions.

In addition to the base line case, a series of parametric analyses considering the effects of armor thickness, chamber radius, and target yield on the first wall response were conducted. These results provide insight into the influence of these parameters on first wall response and allow for extrapolation of these results to other design configurations. To begin with, the armor thickness directly affected the temperatures and stresses in the steel wall as illustrated in Fig. 10. In this figure, the maximum temperatures and stresses in the steel after 50 cycles are plotted as a function of armor thickness. The maximum temperatures and stress magnitudes both decrease with increasing wall thickness as the steel is moved away from the high temperature armor surface. The doubling of the armor thickness from 100 μm to 200 μm, however, reduced the temperature only 19 °C out of a total temperature rise of 147 °C (13%).

The changes in the target yield and chamber radius both influence the first wall response by affecting the fluence entering the wall. The target yield affects the total energy output directly and hence the fluence. For these studies, it was assumed that the fluence varied directly with target yield, and the species fractions and energy spectra were unchanged. Hence, doubling the target yield would double the input energies of each species component while leaving the pulse width unchanged. Because the fluence is the energy deposited per unit area, increasing the chamber radius decreases the fluence

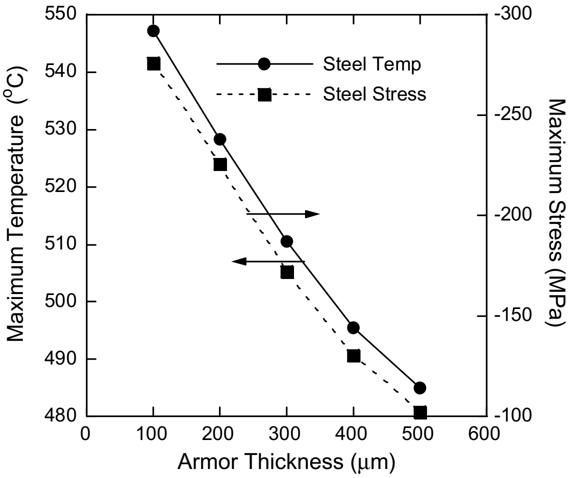

Fig. 10. Maximum temperature and stress in the steel wall as a function of tungsten armor thickness (after 50 target implosions in a 7.0 m radius chamber).

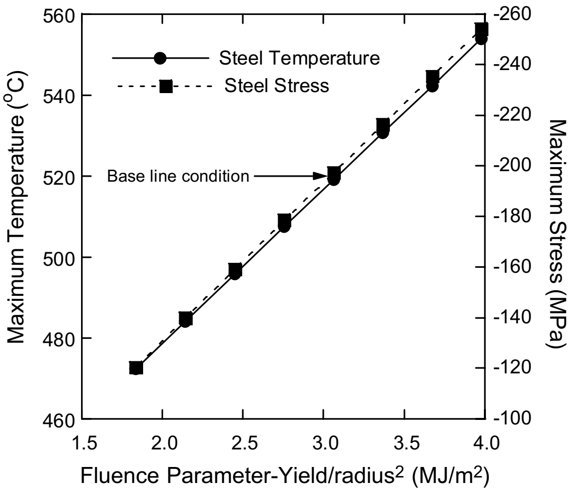

Fig. 11. Maximum temperature and stress in the steel wall as a function of the fluence parameter (after 50 target implosions).

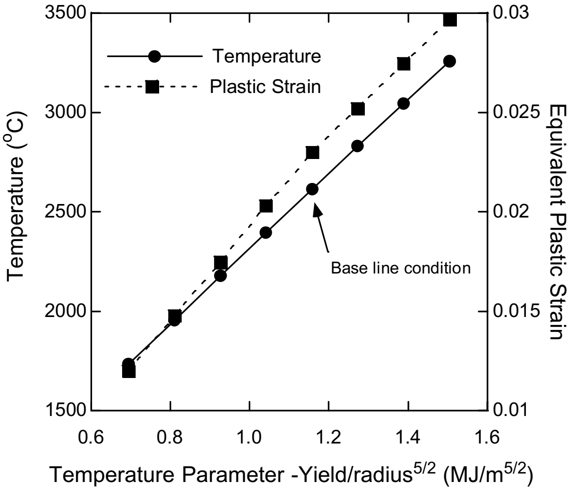

Fig. 12. Maximum temperature and plastic strain at the tungsten armor as a function of the temperature parameter (after 50 target implosions).

by increasing the first wall surface area. For a spherical chamber, surface area is proportional to the square of the radius. The maximum steel temperature and stress were both found to be directly proportional to the fluence for both changes in yield and chamber radius. These data are plotted as function of a fluence parameter, defined as the target yield divided by the square of the chamber radius, in Fig. 11. The base line condition from the previous analyses, a 150 MJ target implosion in the 7.0 m radius chamber, is highlighted in the figure. These data, taken after 50 cycles, indicate a linear relationship between the steel temperature and fluence, and doubling the fluence doubles the temperature rise in the steel.

In addition to the steel temperature and stress, the tungsten armor surface temperature and plastic strain responses to changes in the target yield and chamber radius were investigated. Examining Eq. (1), the surface temperature is not only a function of fluence, but also is a function of the material diffusivity and the pulse width. The material properties are only a weak function of temperature and can be ignored, but the pulse width is directly related to chamber radius for given particle velocities. Hence, the surface temperature is also proportional to one over the square root of the chamber radius as well as the fluence. The finite element predictions of surface temperature and plastic strain were found to correlate to a temperature parameter, defined as the target yield divided by the chamber radius to the five-halves power, for both changes in yield and target radius. The data for both the maximum surface temperature and maximum plastic strain are plotted in Fig. 12, and again the base line condition is indicated. From Figs. 11 and 12, temperatures and structural response in both the steel wall and the tungsten armor can be estimated of a variety of chamber radii and target yields.

6. Fatigue and fracture in armor

The most severe aspect of the loading on the chamber wall is its pulsed nature. A wall will experience more than 10^8 cycles per full power year, resulting in the likelihood of crack growth, particularly in the tungsten coating on the first wall. Hence, the assessment of the viability of the tungsten-coated steel wall design must include a crack growth analysis. In this section we will present a relatively crude analysis based on multiaxial fatigue, along with a more thorough fracture-based analysis.

Fatigue analysis is based on measured data for the life (measured in cycles) of a uniaxial specimen as a function of stress or plastic strain. Because the stress states in the HAPL chamber wall are multiaxial, we must have a model for estimating the lifetime of the multiaxial case using the uniaxial data. There are many such models, but we have chosen to use the following strain-based model [4]. We begin by defining an equivalent strain range as

$$\Delta\varepsilon_{\mathrm{eq}} = \frac{\sqrt{2}}{3}\sqrt{(\Delta\varepsilon_{11}-\Delta\varepsilon_{22})^2+(\Delta\varepsilon_{33}-\Delta\varepsilon_{22})^2+(\Delta\varepsilon_{11}-\Delta\varepsilon_{33})^2+6(\Delta\varepsilon_{12}^2+\Delta\varepsilon_{23}^2+\Delta\varepsilon_{13}^2)}, \tag{8}$$

where

$$\Delta\varepsilon_{ij} = \varepsilon_{ij}(t_1) - \varepsilon_{ij}(t_2)$$

and t_1 and t_2 refer to the times for which the quantity in Eq. (8) is maximized. For our purposes, these times refer to the beginning and end of a heat pulse, since these are the times when the maximum and minimum plastic strains occur. In the case of IFE chamber walls, the strains are biaxial, and the plastic strain is such that there is no change in volume, leading to:

$$\begin{aligned}&\varepsilon_{11} = \varepsilon_{22} = -\frac{1}{2}\varepsilon_{33},\\&\Delta\varepsilon_{\mathrm{eq}} = \Delta\varepsilon_{33}.\end{aligned} \tag{9}$$

Hence, to determine the fatigue life of the chamber wall, one simply calculates the plastic strain range perpendicular to the surface and uses that to compute the lifetime from a uniaxial fatigue curve based on plastic strain range.

The measured fatigue life for tungsten is given in Appendix A. These data are for stress-relieved tungsten at 1232 °C, which is the highest temperature data available. Using these data and the model presented above, the lifetime of the tungsten coating can be estimated for a variety of different operating conditions and coating thicknesses. These results are provided in Fig. 13 as a function of the tungsten surface temperature parameter developed previously in this paper.

These data are presented as the number of cycles to initiate cracks, because as the cracks move away from the tungsten surface, the local stresses near the crack tip will diminish, thus reducing the crack growth rate. Thus, we cannot consider the fatigue results as failure predictions, because it is quite possible that the cracks will stop growing as they progress through the coating, if the loads they encounter are sufficiently reduced. In order to assess this effect, we must move beyond the fatigue analysis and consider a fracture-based approach.

The high stresses near the tungsten surface along with the fatigue calculations indicated that material cracking near the surface of the tungsten is inevitable. To assess the potential for cracks to propagate through the wall, fracture mechanics-based finite element models were developed. These models used the singular crack tip elements and J-integral routines in ANSYS to predict the stress intensity of cracks of various depths. These analyses incorporate models of an existing crack into the full

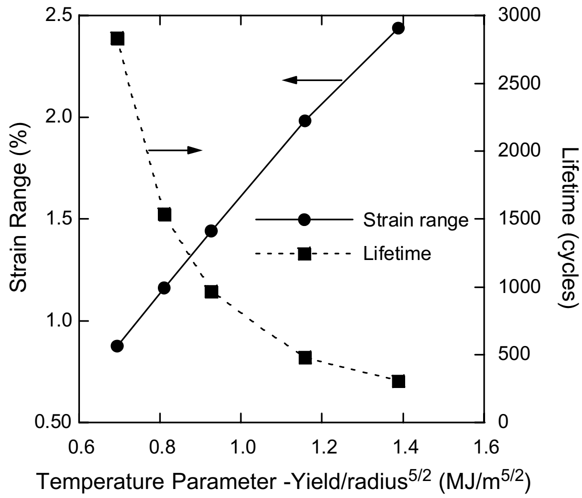

Fig. 13. Predicted strain range and estimated number of cycles to initiate surface cracks in tungsten coating as a function of the surface temperature parameter.

transient, nonlinear thermal and structural analyses of the wall thermal cycle. The primary difference between the previous models and these fracture models is that the fracture models are planar, in order to permit the study of the effect of crack spacing (using symmetry conditions).

The J-integral method was then used to calculate the stress intensity factor at each analysis step. The stress intensity factors could then be compared to the fracture toughness properties of tungsten to determine if the cracks would propagate further. The region of the finite element model containing the crack is shown in Fig. 14. The illustration shows the model in its displaced shape, displacements magnified 10×, at the end of one cycle. A symmetry condition is imposed on the model edge with the crack. One complication of the fracture model for the first wall is that the region with the crack goes into compression during the heating phase. This required the use of contact elements along the crack surface to prevent material overlap along the symmetry plane and greatly increased computational requirements. Along the opposite edge, displacements were coupled in the horizontal direction, producing a symmetry boundary condition which allowed for free net thermal expansion. The symmetry boundary conditions implied the existence of a series of cracks spaced twice the model width from each other, and the results were dependent on model width (or crack spacing).

The transient stress intensities calculated for a 25 μm deep crack in the armor are plotted in Fig. 15. The stress intensity, calculated at each transient structural analysis point, was zero during the portion each pulse when the hot surface was in compression. After the pulse, the stress intensity increased as the surface cooled and the stresses became tensile. The stress intensity increased slightly with each cycle as the gradual heating of the steel substrate increased the tensile stress in the armor. The calculated stress intensity increased from 9.2 MPa $m^{1/2}$ after one pulse to 9.6 MPa $m^{1/2}$ after 20 pulses a 4.4% increase. In order to understand the stress intensity and the potential crack propagation in the armor, a series of analyses were performed for various crack depths and spacings. The analyses all utilized the base line operating condition of a 150 MJ target yield, 7 m chamber radius, and 250 μm armor thickness. Because of the significant computational requirements of each fracture mechanics simulation, the following data are based on the calculated stress intensity after a single pulse cycle. Hence, the data will likely under predict the continuous operation stress intensities by a small fraction.

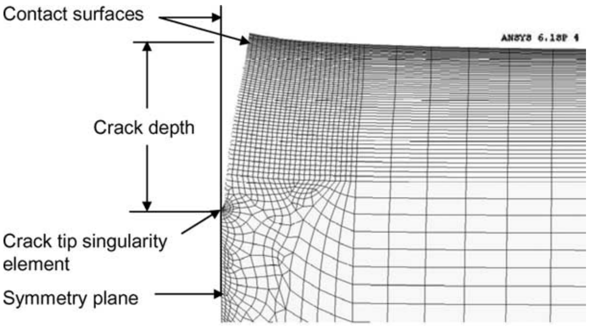

Fig. 14. Deformed FEA model in region of first wall containing a crack.

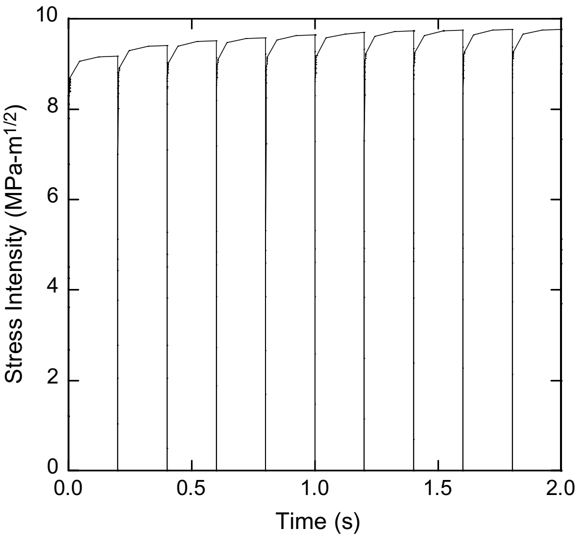

Fig. 15. Transient stress intensity near a 25 μm deep crack in the armor surface subjected to repeated heating pulses.

The ANSYS finite element analyses cannot simulate crack growth, but rather provide the stress intensity for a given crack size which may be compared with the material fracture toughness to determine if a crack would propagate. The stress intensity factor changes with crack depth because of variations in the tungsten stress through the material depth as well as modifications of the crack geometry. Models were generated with crack depths ranging from 15 μm to 150 μm, and the stress intensities were calculated. The results are plotted in Fig. 16. The stress intensity falls from over 10 MPa $m^{1/2}$ for the 15 μm crack to 2.6 MPa $m^{1/2}$

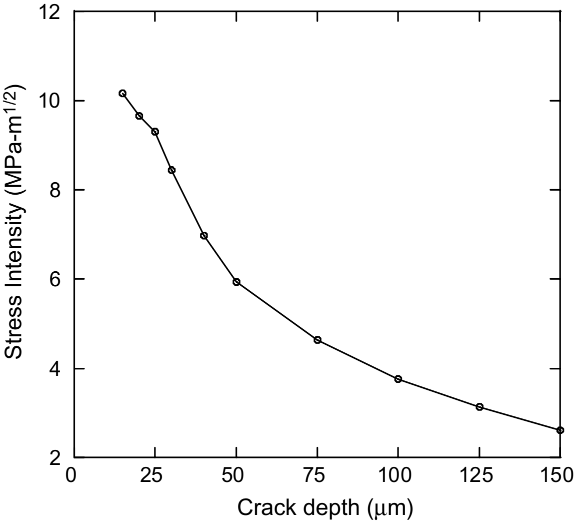

Fig. 16. Variation of fracture stress intensity with crack depth in the tungsten armor. Results after a single pulse with 1 mm crack spacing.

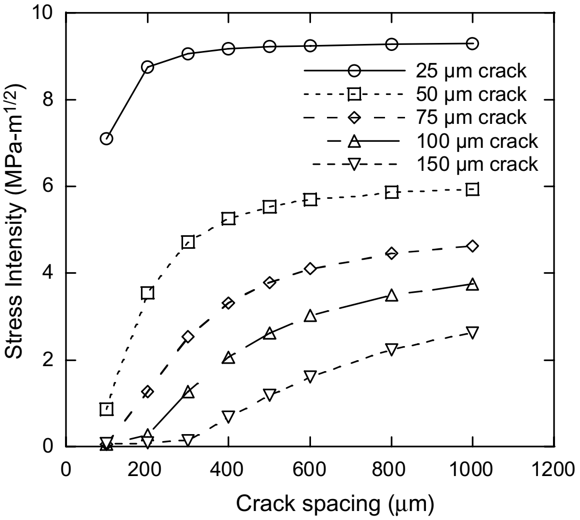

Fig. 17. Variation in fracture stress intensity with crack spacing for several crack depths. Results after a single pulse.

for the 150 µm crack. The reduction in the stress intensity with crack depth indicates that cracks that initiate at the surface may stop before reaching the armor/steel interface. Gumbsch [5] provide fracture toughness data for single crystal tungsten from 100 to 600 K. In all cases, the toughness is over 10 MPa $m^{1/2}$ above 400 K, though it does decrease in the range from 500 to 600 K. Hence, it is not likely that catastrophic failure will occur in the tungsten, and the key concern is cyclic growth during the many cycles to be expected in the HAPL structures.

As noted previously, the stress intensity results are a dependent not only on crack depth but also on crack spacing. The crack spacing is implied by the finite element model width dimension. The presence of additional cracks tends to reduce the tensile stresses at the surface of the armor. The reduction is dependent on both crack size and spacing. The results in Fig. 16 were all calculated with a model that assumed a 1 mm crack spacing. A further series of analyses were performed for crack depths over a range of crack spacings. These results are plotted in Fig. 17. For the 25 and 50 µm deep cracks, the stress intensity appears to have reached a plateau at the 1 mm crack spacing. For the deeper cracks, the stress intensity is still increasing with increasing crack spacing. More importantly, stress intensities drop to nearly zero for deeper cracks with smaller spacings, and a possible scenario would be for a number of closely spaced cracks to initiate at the armor surface where the stress intensities are highest, and the propagation of many or all of these cracks might stop less than 100 µm into the surface. There is limited fracture mechanics data for thin tungsten films, especially when subjected to these extreme temperature cycles, so prediction of fracture behavior is difficult. Data on crack growth rates is needed to make conclusive predictions of the ultimate fate of the cracks.

The crack spacing that reduces the stress intensity is controlled by the stress gradients at the surface. The spacing must be on the order of the characteristic length of the stress variation, which is very shallow for these short pulse situations. With steady state heating, such as is seen in magnetic fusion energy (MFE) first walls, the stresses would vary linearly over the thickness of the wall, so the crack spacing would have to be on the order of the thickness, which is 3 mm in this case. Hence, the required spacing is significantly smaller for IFE walls than for those in MFE.

One issue not addressed here is that of strain rate. The strain rates seen here are on the order of $10^8\ s^{-1}$, and this may affect the tungsten properties. For example, the flow stress of room temperature, polycrystalline tungsten increases by about 50% as the strain rate increases from 10^{-3} to $10^4\ s^{-1}$ [6]. More importantly, the fracture toughness will depend on strain rate. For example, Couque et al. [7] find that the toughness of tungsten heavy alloys drops from 71 to 28 MPa $m^{1/2}$ as the stress intensity loading rate increases from 1 to 10^6 MPa $m^{1/2}$/s. On the other hand, Rittel and Weisbrod [8] find that the toughness of similar tungsten heavy alloys increases with strain rate in some directions. More data for pure tungsten is needed before firm conclusions can be made.

In addition, interface fracture (delamination) is an important element of the performance of this structure. This has not yet been addressed, but we are in the process of developing a model for this phenomenon.

7. Stresses and fatigue in substrate

As with the tungsten coating, one must be concerned about the pulsed nature of the stresses with respect to the steel. In fact, the concern is stronger because while one might imagine tolerating surface cracks in the tungsten, it is difficult to imagine tolerating cracks in the steel. Hence, the primary concern in the steel is high cycle fatigue. Appropriate data is not available for these steels, but there is data [9] for F82H, a reduced activation ferritic steel, at several thousand cycles. This data indicates that stress amplitudes of over 400 MPa will yield lifetimes of well over 100000 cycles. There is no data beyond this cycle level to determine the stresses needed to ensure 10^8 cycles as needed for HAPL. Without data for higher cycles in F82H, we are forced to consider data for other ferritic steels. For example, Kobayashi et al. [10] find that 12Cr–2W ferritic steels have lifetimes over 10^8 cycles at stress amplitudes over 300 MPa at 400 °C, which is a level of over 0.5 times the yield stress. Hence, there is a significant margin in the steel stress levels. This is a conservative analysis, given that the tensile stresses in a typical HAPL cycle are not as high as the compressive stresses, whereas the tests are done with a mean stress of 0.

8. Implications for first wall experiments

Experiments must be used to validate the modeling used in this paper to assess the viability of the tungsten-coated steel design. There are no existing facilities that can precisely duplicate the conditions and threats expected in a laser fusion chamber, so the HAPL project has chosen to conduct five complementary experiments in parallel. Four of these experiments, using lasers, ions, and X-rays, are intended to simulate the conditions of the tungsten surface, while the fifth, using infrared heating, is intended to simulate the conditions of the interface between the tungsten and the steel. The parameters of the surface experiments are given in Table 3. For each of these facilities, the pulse length is significantly shorter than that of the ions in a laser IFE chamber. Hence, we must investigate the implications of these differences with respect to the ability of the experiments to mimic the failure modes in an IFE chamber.

To compare the thermostructural fields in the experiments to that of IFE walls, we will use single pulse finite element analyses for temperature and plastic strain. These analyses, with heat fluxes adjusted to produce proper surface temperatures, are adequate for qualitative comparison, but more detailed analyses will be needed to properly use the experimental data for chamber design. The approach here is to determine the fluence necessary to duplicate the peak temperature expected in an IFE chamber pulse and then compare the temperature and plastic strain through the depth of tungsten at the test and chamber conditions. For comparison, the ion beam and laser simulation conditions were selected with the pulse widths listed in Table 3. The laser energy was deposited as a surface heat flux, and the ion beam energy was deposited over a depth of 1 μm. The temperature and plastic strain distributions near the surface of the tungsten are

Table 3
Parameters of experiments used to simulate the surface temperature fluctuations in a laser fusion first wall

Type	Energy (keV)	Maximum fluence per pulse (J/cm^2)	Depth of energy deposition (μm)	Flat top pulse width (ns)	Maximum rep rate (Hz)
Ion beam	750	7	1–10	100	
Pulsed Z-pinch (X-rays)	0.8–1.2	3000	1–2	6	
Single shot Z-pinch (X-rays)	0.1–0.4	7	1–2	30–50 (FWHM)	10
Laser		0.7	0	8	10

plotted in Figs. 18 and 19. The temperature and plastic strain at the surface can be closely simulated, but the short pulse widths of the test conditions do not allow for accurate simulation of the temperature and strain gradients into the depth. Hence these tests are likely to be more applicable for surface damage rather than the assessment of crack propagation into the depth of the armor.

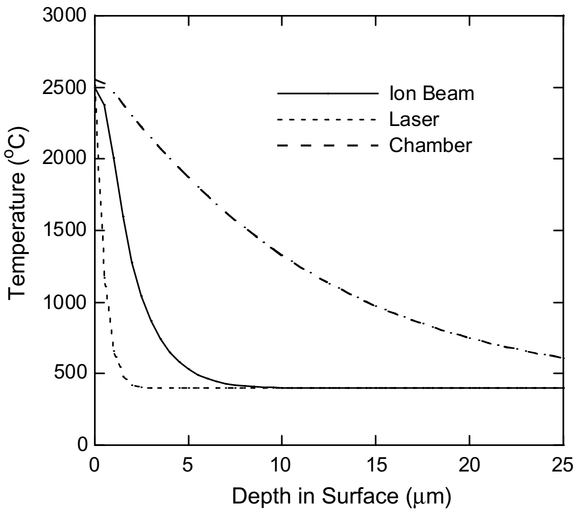

Fig. 18. Temperature distribution near the tungsten surface after heating pulse from ion beam and laser test conditions as compared with predicted chamber conditions.

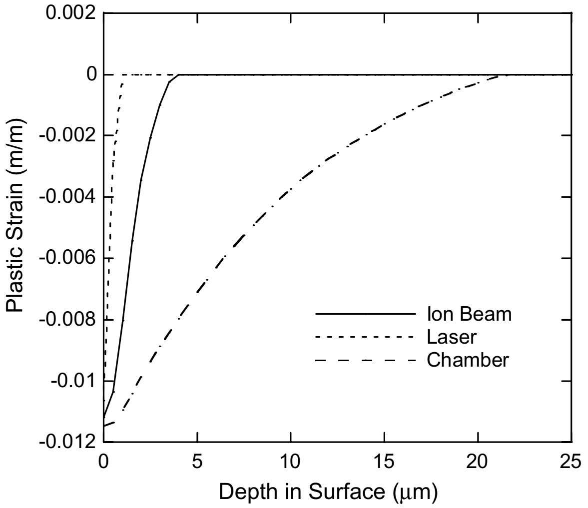

Fig. 19. Plastic strain distribution near the tungsten surface after heating pulse from ion beam and laser test conditions as compared with predicted chamber conditions.

The infrared (IR) experiments will be used to simulate the thermostructural fields in the vicinity of the interface between the tungsten and steel. The pulse length on the IR source here is not short enough to duplicate the steep gradients at the tungsten surface, but the time-averaged power is more than adequate to simulate the bond fields. On the other hand, the surface experiments in Table 3 can duplicate the surface effects, but they do not have adequate time-averaged power to duplicate the bond conditions. Hence, the two approaches are compatible. In these experiments, the IR pulse is on the order of tens of milliseconds, with peak powers of tens of MW/m^2. The exact pulse length, dwell time, and power is chosen to duplicate the chamber conditions as closely as possible.

Finite element calculations have been carried out to compare the experimental temperature and stress to the conditions expected in the HAPL chamber. The IR conditions were 20 ms pulse width, 7.2 MW/m^2 heat flux, and 400 ms dwell time. The coolant for the stage was assumed to be 400 °C water and the heat transfer coefficient was assumed to be 10000 W/m^2 K, the same as in the base line HAPL condition. The temperatures and stresses at the interface and in the steel compared well with the HAPL case. The stresses through the thickness of the armor and steel immediately after a heat pulse are plotted in Fig. 20. These are the times of

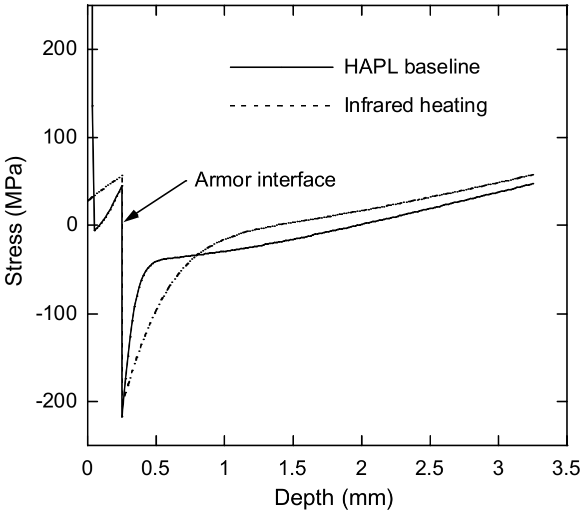

Fig. 20. Thermal stresses distribution through the armor and steel wall thickness after 50th heat pulse for HAPL base line and infrared heating simulation.

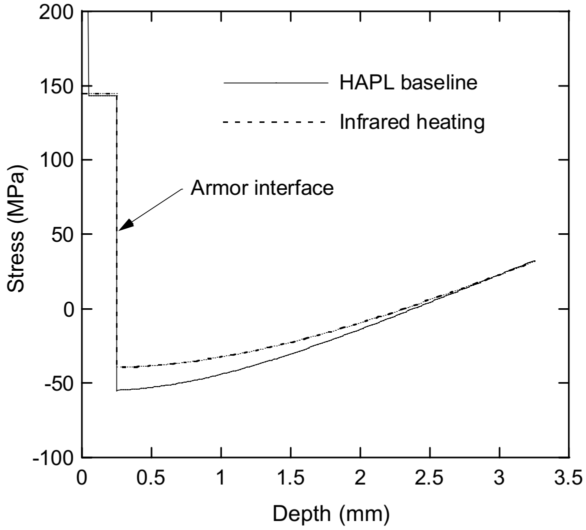

Fig. 21. Thermal stresses distribution through the armor and steel wall thickness prior to 51st heat pulse for HAPL base line and infrared heating simulation.

maximum temperature and stress at the armor to steel interface. The stresses immediately before the next pulse, when gradients are the lowest, are plotted in Fig. 21. These results indicate that the stress ranges in the steel and in the tungsten near the interface can be closely simulated with infrared heating, but the stresses near the tungsten surface cannot.

9. Conclusions

Transient temperatures and stresses have been determined for a tungsten-coated steel wall in a laser fusion chamber. The surface temperatures are found to be well below the tungsten melting temperature for a reasonable target yield and chamber size. In addition, the stresses are found to exceed the yield stress, and the cyclic plastic strains are found to be several percent per cycle. Simple fatigue analysis indicates that surface cracks will be initiated after a few thousand cycles, depending on the target yield and chamber radius. Hence, cracking is unavoidable in any reasonable IFE dry wall chamber employing tungsten coatings. More rigorous fracture analysis indicates that these surface cracks will not necessarily propagate to the tungsten/steel interface. In particular, the cracks are predicted to arrest before reaching the steel if the crack spacing is less than 300 μm and the tungsten thickness is at least 200 μm. Future work will address the important problem of interface fracture. Stresses in the steel are found to be below the values necessary to ensure a lifetime of 10^8 cycles, though this conclusion is based on limited data.

Finally, the thermal and stress fields expected in several experiments intended to duplicate the laser fusion conditions were presented. The simulations all had shorter pulse lengths than the reactor case, so the peak temperatures could be reproduced, but not the depth of the stress distribution.

Acknowledgements

This work was sponsored by the Naval Research Laboratory in support of the High Average Power Laser program.

Appendix A

Thermostructural properties[a]

Property	Units	Formula (T in centigrade)
Tungsten		
Density	(kg/m^3)	$19302.7 - 0.23786 * T - 2.2448\text{E}-5 * T^2$
Heat capacity	(J/kg K)	$128.3 + 0.0328 * T - 3.41\text{E}-6 * T^2$
Thermal conductivity	(W/m K)	$174.9 - 0.107 * T + 5.01\text{E}-5 * T^2 - 7.835\text{E}-9 * T^3$
Elastic modulus	(GPa)	$398 - 0.00231 * T - 2.72\text{E}-5 * T^2$
Poisson's ratio		$0.279 + 1.09\text{E}-5 * T$
Thermal expansion coefficient	(10^{-6} K^{-1})	$3.922 + 5.835\text{E}-5 * T + 5.705\text{E}-11 * T^2 - 2.046\text{E}-14 * T^3$
Tangent modulus	(MPa)	667
Fatigue		Plastic strain range $= 34 * (N_f)^{-0.46}$
Steel		
Density	(kg/m^3)	7800
Heat capacity	(J/kg K)	$500 + 0.6 * T$
Thermal conductivity	(W/m K)	33
Elastic modulus	(GPa)	$230 - 0.05 * T$
Poisson's ratio		0.29

(*continued on next page*)

Appendix A (*continued*)

Thermal expansion coefficient	(10^{-6} K^{-1})	$10 - 0.0025 * T$
Tangent modulus	(MPa)	667

[a] The tungsten properties were all collected from the ITER Materials Handbook, which is available from: <http://aries.ucsd.edu/LIB/PROPS/ITER/AM01/AM01-0000.html>. The steel properties were obtained from Refs. [11,12].

Tungsten yield stress

Temperature (°C)	Yield stress (MPa)
0	1385
500	853
1000	465
1500	204
2000	57
2500	10

Steel yield stress

Temperature (°C)	Yield stress (MPa)
0	950
200	900
400	750
500	600
600	250
800	50

References

[1] J.D. Sethian et al., J. Nucl. Mater., these Proceedings, doi:10.1016/j.jnucmat.2005.08.019.

[2] J. Blanchard, Fus. Sci. Tech. 44 (1) (2003) 101.

[3] H. Carslaw, J. Jaeger, Conduction of Heat in Solids, Oxford Clarendon, 1959.

[4] Y.S. Garud, J. Test. Eval. 9 (3) (1981) 165.

[5] Peter Gumbsch et al., Science 282 (1998) 1293.

[6] T. Dummer et al., Acta Mater. 46 (17) (1998) 6267.

[7] H. Couque, J. Lankford, A. Bose, J. Phys. III 2 (1992) 2225.

[8] D. Rittel, G. Weisbrod, Int. J. Frac. 212 (2001) 87.

[9] J.S. Stubbins, D.S. Gelles, J. Nucl. Mater. 233–237 (1996) 331.

[10] K. Kobayashi, K. Yamaguchi, M. Kimura, M. Hayakawa, J. Mater. Sci. 39 (2004) 6253.

[11] R.L. Klueh, et al., Fusion Materials – Semiannual Progress Report – DOE/ER-0313/28, 28, 2000, p. 123.

[12] K. Shiba, N. Yamanouchi, A. Tohyama, Fusion Materials – Semiannual Progress Report – DOE/ER-0313/20, 20, 1996, p. 190.